Semiconductor Physics, Quantum Electronics & Optoelectronics, 2017. V. 20, N 3. P. 355-361.

PACS 61.05

Modeling of X-ray rocking curves for layers after two-stage ion-implantation

O.I. Liubchenko, V.P. Kladko, O.Yo. Gudymenko
V. Lashkaryov Institute of Semiconductor Physics, NAS of Ukraine,
41, prospect Nauky, 03028 Kyiv, Ukraine;
e-mail: lubchenco.a@gmail.com

Abstract. In this work, we consider the approach for simulation of X-ray rocking curves inherent to InSb(111) crystals implanted with Be^+ ions with various energies and doses. The method is based on the semi-kinematical theory of X-ray diffraction in the case of Bragg geometry. A fitting procedure that relies on the Hooke–Jeeves direct search algorithm was developed to determine the depth profiles of strain and structural disorders in the ion-modified layers. The thickness and maximum value of strain of ion-modified InSb(111) layers were determined. For implantation energies 66 and 80 keV, doses 25 and 50 μC, the thickness of the strained layer is about 500 nm with the maximum value of strain close to 0.1%. Additionally, an amorphous layer with significant thickness was found in the implantation region.

Keywords: X-ray rocking curve modeling, two-stage implantation, Hooke-Jeeves direct search, strain distribution.

Manuscript received 18.08.17; revised version received 04.09.17; accepted for publication 00.00.17; published online 00.00.17.

1. Introduction

Output characteristics of nano- and microelectronic devices strongly depend on technological processes during their fabrication. Therefore, it is important to investigate the influence of each technological step on the device characteristics. Accurate investigation of the clue technologies such as ion implantation, diffusion and passivation, allows to control the electro-physical parameters of the devices [1–5].

Ion implantation is a widely used technique for fabrication of variety of nano- and microelectronic devices [1, 2, 6]. This method allows to introduce impurities with preset concentration profiles without use of elevated temperatures, and is mostly used for *p*- or *n*-type doping [3–5]. Investigation of its influence on structural changes in the post-implanted material will allow to improve the output characteristics of these devices, which is of great importance.

X-ray diffraction (XRD) is a widely used technique for nondestructive structural characterization of semiconductor materials. For ion-modified layers, the structural changes can be qualitatively investigated by analyzing the X-ray diffraction curves in the Bragg geometry. In addition, simulation of X-ray diffraction curves can be used for the depth profiles of strain determination [7–9]. However, for the ion-modified structures, simulation of XRD spectra is a difficult task with ambiguous solutions [10–12]. The uncertainty arises due to interference of X-rays on heterogeneities of the structure, in particular, in amorphous layer [13, 14].

The kinematical [13–18] and generalized dynamical theory [21, 22] of X-ray diffraction were used in combination with the dynamical approach in case of the Takagi–Topens approximation [11, 12, 19, 20], for the $\omega/2\Theta$ scans simulation for ion implanted layers. The kinematical and the dynamical approaches are used for thin implanted layers and high-quality bulk material,

respectively. To perform this simulation, the ion-modified layer was separated by several sublayers with mean values of strain, defects and clusters concentration. The parameters of each layer were changed, until a good fit between the calculated and measured XRD spectra was achieved.

Many authors [10–17, 19, 20] simulate only the coherent part of the scattered intensity, which gives information about the strains and composition. The diffuse scattering sufficiently complicates the model and is not considered here. In this work, the strain distribution in ion implanted InSb(111) crystals were investigated by means of X-ray ω/2Θ scans simulation.

2. Experimental

Two-stage implantation with Be^+ ions was performed for two series of InSb (111) samples with the same parameters, to check the reproducibility of the experiment. The implantation energies (E) and doses (D) were E = 66 keV and D = 25 μC for the first stage of implantation, and E = 80 keV, D = 50 μC for the second stage. The implantation was carried out through a thin SiO_2 mask layer to avoid the effect of substrate (surface) destruction. More high-energy implantation was carried out to create *p-n* junction in a single InSb crystal, and the second serves as a heteromaper for defects.

The structural parameters of as-implanted samples were examined with high-resolution X-ray diffraction using the PANalytical X'Pert Pro MRD XL diffractometer. The ω/2Θ scans of symmetric (111) and (333) reflections were measured. The X-ray reflectivity measurements were performed additionally to estimate the thickness (~90 nm) of the SiO_2 layer.

3. The model

We use the kinematical and dynamical theories of X-ray diffraction [13–15, 23, 24] to simulate the X-ray ω/2Θ scans for the Be^+ implanted InSb layer and substrate, respectively. The kinematical theory is feasible for the ion-implanted layer because of its small thickness and high structural disorder. Proper simulation of the intensity scattered from the high quality InSb substrate should be performed with consideration of the diffuse component of X-ray scattering. However, to keep the model simple we will not consider the diffuse part in our simulations. The general expressions of the semi-kinematical theory of X-ray diffraction are given below.

The reflectivity of the whole structure is proportional to the reflection amplitude of the substrate (A_0) and layer (A_L)

$$R = \left|A_0 + i \cdot A_L\right|^2, \tag{1}$$

$$A_0 = \left|\left|y\right| - \sqrt{y^2 - 1}\right|, \tag{2}$$

$$A_L = \sum_{i=1}^{n} a_i \cdot \frac{\sin\left(\left(y - f_i\right) \cdot u_i\right)}{y - f_i} \cdot \exp\left(-i \cdot \phi_i\right), \tag{3}$$

where ϕ_i is the phase, y – angular deviation, f_i, u_i and a_i are the normalized strain, thickness and absorption multiplier in the i-th layer.

$$\phi_i = \left(y - f_i\right) \cdot u_i + \sum_{k=1}^{i-1} 2 \cdot \left(y - f_k\right) \cdot u_k, \tag{4}$$

$$y = \frac{\Delta\Theta \cdot \sin\left(2\Theta\right)}{\left|\chi_H\right|} \sqrt{\frac{\gamma_0}{\left|\gamma_H\right|}}, \tag{5}$$

$$f_i = -\varepsilon_{zz}^i \cdot \frac{\left(\gamma_H - \gamma_0\right) \cdot \gamma_H}{\left|\chi_H\right|} \sqrt{\frac{\gamma_0}{\left|\gamma_H\right|}}, \tag{6}$$

$$u_i = \frac{\pi \cdot t_i \cdot \left|\chi_H\right|}{\lambda \cdot \sqrt{\left|\gamma_H\right| \cdot \gamma_0}}, \tag{7}$$

$$a_i = \exp\left(-\mu \cdot \frac{\gamma_0 + \left|\gamma_H\right|}{2 \cdot \left|\gamma_0 \cdot \gamma_H\right|} \cdot \sum_{j=i+1}^{N} t_j\right) \tag{8}$$

where γ_0, γ_H are direction cosines, $\Delta\Theta$ is angular deviation of the investigated crystal from its exact substrate Bragg position, t_i, ε_{zz}^i are thickness and strain of the i-th layer, Θ_0 is the Bragg angle of substrate, χ_H – Fourier component of the perfect crystal polarizability, λ = 0.1546 nm – X-ray wavelength, μ – absorption coefficient.

The strain distribution in the implanted layers is described with a two-sided Gaussian function [11–13, 15]. It is determined by only four parameters in contradistinction to B-spline basis functions [18, 24, 25]. In our case of two-stage implantation, the strain distribution in the InSb:Be^+ layers is described by a sum of two asymmetric Gaussians:

$$\frac{\Delta d}{d} = \begin{cases} \tau_1 \cdot \exp\left(-\left(\dfrac{x - \rho_1}{2 \cdot \sigma_{11}}\right)^2\right), & 0 < x < \rho_1 \\ \tau_1 \cdot \exp\left(-\left(\dfrac{x - \rho_1}{2 \cdot \sigma_{12}}\right)^2\right), & x > \rho_1 \end{cases} + \begin{cases} \tau_2 \cdot \exp\left(-\left(\dfrac{x - \rho_2}{2 \cdot \sigma_{21}}\right)^2\right), & 0 < x < \rho_2 \\ \tau_2 \cdot \exp\left(-\left(\dfrac{x - \rho_2}{2 \cdot \sigma_{22}}\right)^2\right), & x > \rho_2 \end{cases} \tag{9}$$

where τ_i and ρ_i are the maximum value of strain and its depth, respectively, and σ_{i1}, σ_{i2} – full widths at half maximum of the *i*-th Gaussian function.

Principles of the program developed for the ω/2Θ scans simulation are reviewed below. The program is written using the C^{++} programming language (https://gcc.gnu.org/) and parallel computing platform CUDA (https://developer.nvidia.com/cuda-toolkit). The input data are the parameters of 2 asymmetric Gaussians, the experimental ω/2Θ scan and the characteristics of material. The simulation procedure is as follows: (1) reading the input data; (2) calculating strain distribution and intensity of scattering by the structure; (3) convolution of the calculated ω/2Θ scan with the instrumental function (instrumental function is approximated by the Gaussian profile with full width at half maximum (FWHM) 12 arc sec that is responsible for the FWHM of an analyzer's rocking curve); (4) additional convolution is carried out for rough search of optimal parameters [11]; (5) determination of the mean error between experimental and calculated data by using the equations (10), (11); (6) performing the fitting, which consists of multiple repeating the steps 2 to 5 with using the minimization algorithm; (7) after the minimum error is found, the program saves and shows the profiles of strain distribution, calculated data, and finishes its work.

The Nelder–Mead Algorithm [26] and Hooke–Jeeves Direct Search ("pattern search") [27] were applied for error minimization in our simulation. Both methods are unconditional, and function minimization is performed by setting the starting point to search for a minimum (or maximum). Also, these algorithms have no required derivatives of the error function; only the value of the function is required. Finding the derivative in our case would be a complicate problem. Also, we note that these methods can find only the local minimum. To find the global minimum, one must set different starting points, or as in our case, use additional convolution.

The Nelder–Mead method, or the amoeba method, is the commonly applied numerical method used to find the minimum or maximum of an objective function in a multidimensional space. The method uses the concept of a simplex, which is a special polytope of n+1 vertices in n dimensions. Based on the values calculated in the vertices of the simplex, the search for the minimum value is performed using reflection, compression and stretching operations. When the distance between the vertices of the simplex decrease less than to a certain value, there is an exit from the procedure (checking for convergence). In detail, the principle of the algorithm is described in [26, 28]. The fitting of X-ray ω/2Θ scans is performed to fulfill the condition of convergence or to exceed the number of iterations. We used a ready-made algorithm for applied statistics AS 047 [29].

Hooke–Jeeves Direct Search, also known as pattern search, is a family of numerical optimization methods. It consists of two stages: the exploratory move and the pattern move. At the first stage, the starting point 1 and the steps for each coordinate should be defined. Then, the values of all coordinates are fixed except for the first one, and values of the function in points at the step distance from the initial value are found. Next, the transition to the point with the smallest value of the function is performed. If the value at the starting point is less than the values for both directions of the step, then the step in this coordinate decreases. This procedure is performed for all coordinates to a given minimum. In this way, we obtain a new point with the smallest value of the function in the neighborhood (denote its 2). At the second stage, the point 3 is set aside in the direction from 1 to 2 at the same distance. Then, at point 3, the exploratory move is performed without decreasing the step. If the point 4 another than 3 is given, then there is a redefinition of the points: 2→1, 4→2; else there is a redefinition of the point 2→1 and repeat an exploratory move. The minimum search is performed until the shift step in all coordinates will not be less than the given value or to exceed the number of iterations. In our work, we used the modified Hooke–Jeeves algorithm [30].

The Nelder–Mead algorithm works faster, but when some precision of the fit is reached, this method "stagnates" and, despite the built-in convergence check, the exit from the procedure is carried out on the condition of the iterations' number. To improve the accuracy of the solution, one needs to set more iterations, which is time consuming. Hooke–Jeeves direct search works slower, but fitting quality is better than in the previous method. On average, the number of attempts to minimize errors by using the Hook–Jeeves method was smaller. In general, the behavior of both algorithms at a rough search minimum is similar. When one set different starting points far from the global minimum, there are often local minima, which points to a complex profile of errors. Therefore, Hooke–Jeeves algorithm for fitting of X-ray diffraction spectra was more applicable. This may be caused by the complicated hyper surface profile of the error function, depending on the many parameters or the fact that the optimization parameters are interrelated (*e.g.*, σ_1, σ_2 – half-widths of the asymmetric Gaussian, which give a similar contribution to the diffraction pattern).

It was ascertained that applying the Hooke–Jeeves method, the best fit was achieved when using the mean error function given by the expression:

$$Err = \frac{1}{N}\sum_{i=1}^{N}\frac{\left| I_i^{theor} - I_i^{exp} \right|}{I_i^{exp}}, \qquad (10)$$

where N is the number of experimental points on the X-ray spectra; I_i^{theor} and I_i^{exp} are the calculated and experimental intensities, respectively.

For the Nelder–Mead algorithm, the best fitting was achieved when using the following mean error function:

$$Err = \sum_{i=1}^{N} \left| I_i^{theor} - I_i^{exp} \right|. \quad (11)$$

The intensity scattered from the layer was calculated using Eq. (3). Herewith, the layer was separated by *n* sublayers. Investigation of the effect of the number of sublayers on the diffraction pattern showed that with the number of sublayers higher than 50, there were no significant changes in the calculated spectrum. However, for our fitting procedure the number of sublayers has been increased up to 200. The depth profile of strain in the ion-implanted InSb layer was calculated using Eq. (9). It is important to calculate it by choosing the point where one can ignore the strain (*i.e.*, the boundary between the layer and the substrate), which affects the X-ray spectrum near the substrate peak. We assume that the strain of about 1% of the maximum value has a minor effect on the X-ray spectrum and can be neglected in simulation. This decrease of strain can be observed at a distance of about $4.3\sigma_{1i}$ from the maximum value.

4. Results and discussion

Simulation of the whole spectra has shown violation of the peaks intensity ratio between the layer and substrate. Without convolution with instrumental function, this difference is about one order of magnitude. When using convolution, it depends on the width of the window of convolution. Most likely, this is because we used the semi-kinematical approach without consideration of the static Debye–Waller (DW) factor. Therefore, an additional fitting parameter was introduced in the model, which multiplies the intensity reflected from the substrate. With a decrease of this factor, the intensity fluctuations in the interference pattern from the layer become better visible. The fact that the value of the intensity adjustment coefficient has a roughly identical value for the whole layer can indicate a homogeneous amorphization of this layer. Also, the fitting procedure works far better in the case of fitting the part of spectrum that corresponds to the layer, so we did not adjust the part of the spectrum containing the substrate peak at an exact Bragg angle. When the fitting of the whole spectrum was conducted, the best result was achieved using the error function (Eq. (11)), but there are oscillations of intensity and poor coincidence of the "tails" between the calculated and experimental ω/2Θ scans. So, we used the error formula (Eq. (10)) and simulated only the part of spectrum that corresponds to the implanted layer.

For the sample 1, we simulated the ω/2Θ scans of (111) (Fig. 1a) and (333) reflections (Fig. 1b). This simulation was carried out using the above described algorithm. The top SiO_2 mask layer was not taken into account in this simulation for the following reasons: after the ion implantation, this layer can be considered as amorphous, which contributes to the diffuse component of the X-ray spectra. However, we do not consider the diffuse component in our model, and calculate only the coherent part of the X-ray scattering. The obtained depth profiles of strain have been compared in Fig. 1c, and some differences in the profiles obtained from simulation of ω/2Θ scans for (111) and (333) reflections are observed. It should be noted that we expect more accurate determination of the depth profile of strain when simulating the ω/2Θ scan of the high-order (333) reflection as compared with the ω/2Θ scan of (111) reflection. First, the lower order reflections are less strain sensitive. Secondly, the ω/2Θ scans of these reflections do not have well-defined features, and thirdly, the peak of the layer is close to the peak of substrate. All of this increases the error of the strain profiles determination from the ω/2Θ scans fitting for lower-order reflections.

Fig. 2a shows the depth profiles of strain in the sample 2 determined by simulating the ω/2Θ scans of both (111) and (333) reflections. For each reflection, the strain profiles were obtained by specifying different starting points in the fitting algorithm to achieve the minimum fitting error (Eq. (10)). Noticeable differences between the strain profiles obtained from simulation of the (111) and (333) reflections can be observed, too.

Fig. 2b compares the depth profiles of strain for both samples. Despite the same designed conditions of the ion implantation, there are some differences between the obtained profiles of strain distribution. The strain profiles obtained from the less sensitive reflection (111) almost coincide for both samples. The deformation profiles obtained from the reflection (333) show a greater thickness of the strained layer for the sample 1, indicating a greater energy of implantation. There are also some differences in the strain distribution near the surface. This indicates that the real parameters of the implantation process are not fully repeatable for the samples 1 and 2.

For each ω/2Θ scan, the average fitting error do not exceeds 10%. Finishing the fitting algorithm was carried out, when the step $\delta = 10^{-8}$ was reached. The difference in the depth profiles of strain obtained by simulating the ω/2Θ scan of (111) and (333) reflections is explained by the ambiguity of modeling these structures. For example, different shapes of the strain profile can lead to similar changes of the X-ray spectra. By taking into account the absorption (attenuation) of X-rays can simplify the task to determine strain profiles. However, it requires the use of more advanced models that are more complicated and require longer computational time.

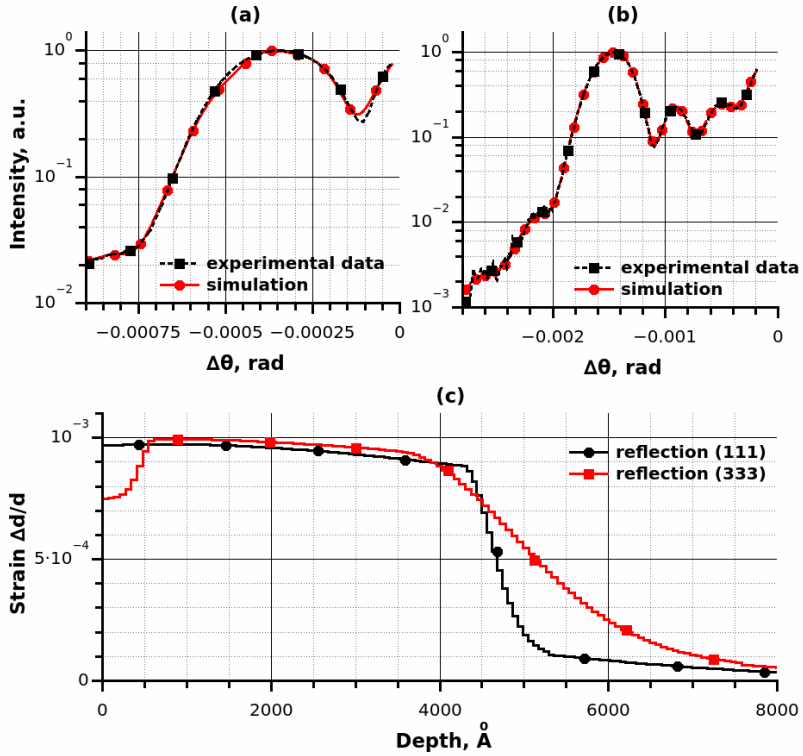

Fig. 1. The measured (black squares) and simulated (red circles) ω/2Θ scans of (111) (*a*) and (333) (*b*) reflections for the sample 1 (*c*) with the depth profiles of strain obtained from this simulation.

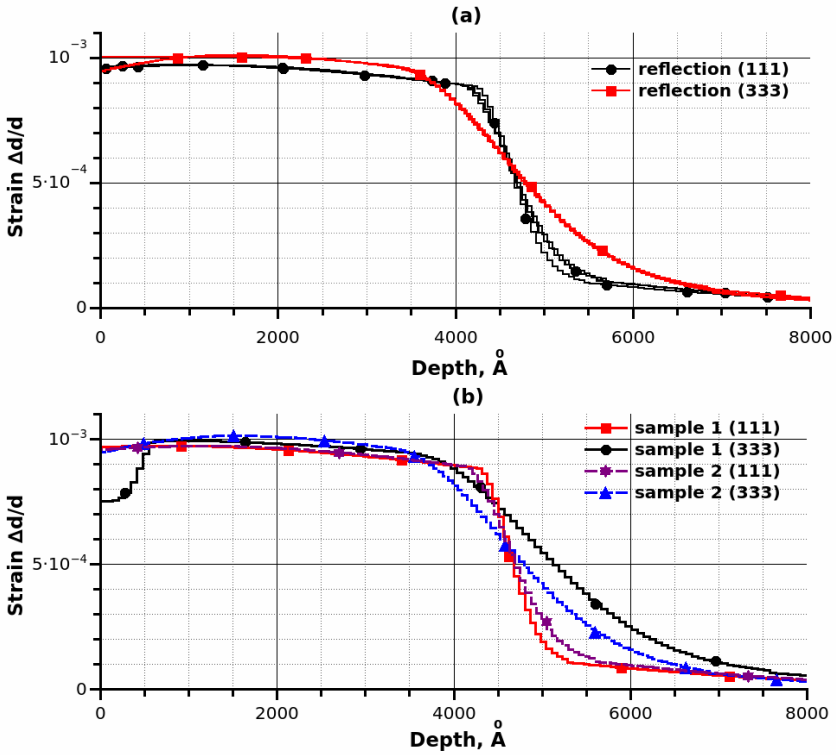

Fig. 2. The depth profiles of strain in the sample 2 obtained from simulation of the ω/2Θ scans for (111) (red squares) and (333) (black circles) reflections (a) and the depth profiles of strain for the samples 1 and 2 obtained from this simulation of ω/2Θ scans for (111) and (333) reflections (b).

5. Conclusions

In this work, we developed the method to simulate the X-ray ω/2Θ scans by using the semi-kinematical theory of X-ray diffraction in the Bragg geometry for two-stage ion-implanted layers. The fitting method is developed on the basis of the Hooke–Jeeves Direct Search algorithm for determining the depth profiles of strain in the implanted layers. The as-implanted layer thickness of InSb was established to be about 500 nm, and the maximum value of strain was ~0.1%. The presence of amorphization in the strained layer was also ascertained. The obtained strain profiles of 2 samples show reproducibility of the implantation process, although slight difference can be observed.

References

1. Dufour C. and Toulemonde M. *Ion Beam Modification of Solid.* Springer Series in Surface Sciences, vol 61. Springer, Cham.
2. Crowder B.L., *Ion Implantation in Semiconductors*. Springer, Berlin, Heidelberg, 1971.
3. Melnik V., Popov V., Kruger D., and Oberemok O. AES and XPS characterization of TiN layers formed and modified by ion implantation. *Semiconductor Physics, Quantum Electronics and Optoelectronics.* 1999. **2**, No. 3. P. 81–85.
4. Gamov D.V., Gudymenko O.I., Kladko V.P. *et al*. Research of recombination characteristics of Cz-Si implanted with iron ions. *Ukr. J. Phys*. 2013. **58**, No. 9. P. 881–887.
5. Oberemok O.S.; Litovchenko V.G.; Gamov D.V. *et al*. Formation of silicon nanoclusters in buried ultra-thin oxide layers. *Semiconductor Physics, Quantum Electronics and Optoelectronics.* 2011. **14**, No. 3. P. 269–272.
6. *Ion beam applications in surface and bulk modification of insulators*. International Atomic Energy Agency, 2008.
7. Kladko V., Kuchuk A., Lytvyn P. *et al*. Substrate effects on the strain relaxation in GaN/AlN short-period superlattices. *Nanoscale Res. Lett.* 2012. **7**, No. 1. P. 289-298.
8. Kladko V.P., Kuchuk A.V., Safryuk N.V. *et al*. Mechanism of strain relaxation by twisted nanocolumns revealed in AlGaN/GaN heterostructures. *Appl. Phys. Lett.* 2009. **95**. P. 031907.
9. Kladko V.P., Kuchuk A.V., Safryuk N.V. *et al*. Influence of template type and buffer strain on structural properties of GaN multilayer quantum wells grown by PAMBE, an x-ray study. *J. Phys. D: Appl. Phys.* 2011. **44**. P. 025403.
10. Klappe J.G.E., Bársony I., Liefting J.R., and Ryan T.W. Optimization of ion implantation damage annealing by means of high-resolution X-ray diffraction. *Thin Solid Films*. 1993. **235**, No. 1–2. P. 189–197.
11. Klappe J.G.E. and Fewster P.F. Fitting of rocking curves from ion-implanted semiconductors. *J. Appl. Crystallogr*. 1994. **27**, No. 1. P. 103–110.
12. Bleicher L., Sasaki J.M., Orloski R.V., Cardoso L.P., Hayashi M.A., and Swart J.W. IonRock: Software for solving strain gradients of ion-implanted semiconductors by X-ray diffraction measurements and evolutionary programming. *Comput. Phys. Commun*. 2004. **160**, No. 2. P. 158–165.
13. Milita S., Servidori M. X-ray rocking-curve analysis of crystals with buried amorphous layers. Case of ion-implanted silicon. *J. Appl. Crystallogr.* 1995. **28**, No. 6. P. 666–672.
14. Milita S. and Servidori M. Damage in ion implanted silicon measured by x-ray diffraction. *J. Appl. Phys*. 1996. **79**, No. 11. P. 8278–8284.
15. Kyutt R.N., Petrashen P.V., and Sorokin L.M. Strain profiles in ion□doped silicon obtained from X□ray rocking curves. *phys. status solidi*. 1980. **60**, No. 2. P. 381–389.
16. Speriosu V.S. Kinematical x□ray diffraction in non-uniform crystalline films: Strain and damage distributions in ion□implanted garnets. *J. Appl. Phys*. 1981. **5**, No. 10. P. 6094–6103.
17. Bartels W.J., Hornstra J., and Lobeek D.J.W. X-ray diffraction of multilayers and superlattices. *Acta Crystallogr. A*. 1986. **42**, No. 6. P. 539–545.
18. Boulle A. and Debelle A. Strain-profile determination in ion-implanted single crystals using generalized simulated annealing. *J. Appl. Crystallogr.* 2010. **43**, No. 5. P. 1046–1052.
19. Hill M.J., Tanner B.K., Halliwell A.G., and Lyons M.H. Simulation of X-ray double-crystal rocking curves of multiple and inhomogeneous heteroepitaxial layers. *J. Appl. Crystallogr*. 1985. **18**, No. 6. P. 446.
20. Lagomarsino S., Giannini C., Guagliardi A., Cedola A., Scarinci F., and Aruta C. An automatic analysis of strain-depth profile in X-ray microdiffraction. *Phys. B: Condens. Matter.* 2004. **353**, No. 1–2. P. 104–110.
21. Olikhovskii S.I., Molodkin V.B., Skakunova O.S. *et al*. Dynamical X-ray diffraction theory: Characterization of defects and strains in as-grown and ion-implanted garnet structures. *phys. status solidi*. 2017. **254**, Issue 7. P. 1600689.
22. Yefanov O.M. and Klad'ko V.P. The solution of the dispersion equation in an explicit format for the case of two strong waves. *Metallofizika i Noveishie Tekhnologii*. 2006. **28**, No. 2. P. 227–244 (in Russian).
23. Molodkin V.B., Nizkova A.I., Shpak A.P. *et al*. *Diffractometry of Nanodimensional Defects and Heterolayers of Crystals*. Kyiv, Akademperiodyka, 2005 (in Russian).

24. Souilah M., Boulle A., and Debelle A. RaDMaX: a graphical program for the determination of strain and damage profiles in irradiated crystals. *J. Appl. Crystallogr.* 2016. **49**, No. 1. P. 311–316.
25. Boulle A., Conchon F., and Guinebretière R. Strain profiles in thin films: influence of a coherently diffracting substrate and thickness fluctuations. *J. Appl. Crystallogr.* 2009. **42**, No. 1. P. 85–92.
26. Nelder J.A. and Mead R. A simplex method for function minimization. *Comput. J.* 1965. **7**, No. 4. P. 308–313.
27. Hooke R. and Jeeves T.A. “Direct Search” solution of numerical and statistical problems. *J. ACM*. 1961. **8**, No. 2. P. 212–229.
28. Press W.H., Flannery B.P., Teukolsk S.A., and Vetterling W.T. *Numerical Recipes – The Art of Scientific Computing*. Cambridge University Press, 1986.
29. O’Neill R., Algorithm AS 47: Function minimization using a simplex procedure. *Appl. Stat.* 1971. **20**, No. 3. P. 338–345.
30. Kaupe A.F., Algorithm 178: direct search. *Commun. ACM*. 1963. **6**, No. 6. P. 313–314.